Mechanistic Probes of Zeolitic Imidazolate

Framework for Photocatalytic Application

Brian Pat tengale, a Sizhuo Yang, Sungsik Lee, Jier Huang \*\*

<sup>a</sup>Department of Chemistry, Marquette University, Milwaukee, Wisconsin, 53201

<sup>b</sup>X-ray Science Division, Argonne National Laboratory, Argonne, Illinois, 60349

#### **ABSTRACT**

In this work, we report a zeolitic imidazolate framework (ZIF-67) with remarkable activity for hydrogen evolution reaction (HER) of 40,500 µmol H<sub>2</sub>/g MOF, which is, to the best of our knowledge, the highest activity achieved by any MOF system. This result necessitated assessment of its atomic-scale mechanistic function for HER using advanced spectroscopy techniques including time-resolved optical (OTA) and in situ X-ray absorption (XAS) spectroscopy. Through the correlation of OTA results with catalytic performance, we demonstrated that the electron transfer (ET) rather than energy transfer (ENT) pathway between photosensitizer and ZIF-67 is the key factor that controls the efficiency of HER activity, as HER activity that undergoes ET pathway is 3 orders of magnitude higher than that of ENT process. Using in situ XAS, we unraveled the spectral features for key intermediate species which are likely responsible for the

rate determining process under turn over conditions. This work represents an original approach to study porous ZIF materials at the molecular level using advanced spectroscopic techniques, providing unprecedented insights into the photoactive nature of ZIF frameworks.

**KEYWORDS** MOFs; catalytic mechanism; H<sub>2</sub> evolution reaction; ultrafast spectroscopy; Synchrotron

## 1. Introduction

Zeolitic imidazolate frameworks (ZIFs), a novel subclass of metal organic frameworks (MOFs), have recently attracted extensive attention due to their potential applications in many areas such as gas separation and storage, 1-5 chemical sensors, 6,7 and catalysis. 8-11 They are particularly interesting for catalysis owing to their exceptional chemical and thermal stabilities and variety of imidazolate derivatives, providing a versatile platform for designing robust and efficient ZIF catalysts. 5 Indeed, ZIFs have been exploited as heterogeneous catalysts for various reactions, such as the Knoevenagel reaction, 10,12 transesterification, 13 Friedel-Crafts acylation reaction, 14 oxidation and epoxidation, 15-19 gas phase CO oxidation and hydrogenation, etc. 20,21

Besides these early stage developments that demonstrate the promise of ZIFs as important catalytic materials, recent interests, driven by the need for solar fuel sources and environmental concerns, have extended their applications into the realm of photocatalysis. For example, after embedding photoactive species into the cavity, ZIFs have been used as photocatalysts for dye<sup>22</sup> and phenol<sup>11</sup> degradation. In the presence of photosensitizers, ZIF-9 (composed of Co<sup>II</sup> and benzimidazole) has been used as photocatalysts for CO<sub>2</sub> reduction.<sup>23,24</sup> Very recently, we have also demonstrated that ZIF-67 (composed of Co<sup>II</sup> and 2-methylimidazole) have intrinsic photoactivities

for hydrogen evolution reaction (HER) through the formation of a long-lived intermediate state following energy transfer process from a molecular photosensitizer.<sup>25</sup>

While these studies certainly imply the potential application of ZIFs in photocatalysis, the catalytic activities of these systems are not impressive compared to other Co based HER catalysts. <sup>26-28</sup> Given the multiple advantages of ZIFs as catalysts that can provide unique means to engineer efficiency and selectivity, there is an urgent need to further develop these materials for photocatalytic applications. Progress in this endeavor clearly will require intimate knowledge of the mechanistic origins that guide light harvesting, charge separation, and HER kinetics during the photoinduced catalytic reaction, yet no experimental probes into these mechanistic functions are available to date. In this work, we report the first real-time spectroscopic study on atomic-scale mechanism of ZIF-67 that can efficiently catalyze HER in the presence of [Ru(bpy)<sub>3</sub>]<sup>2+</sup> (bpy = 2,2'-bipyridine) photosensitizer. Specifically, we examined the light harvesting and charge separation dynamics using time-resolved optical transient absorption (OTA) spectroscopy, and investigated structure-function relationship of ZIF-67 under standard photocatalytic conditions using in situ X-ray absorption spectroscopy (XAS). Using OTA, we found that efficient electron transfer (ET) rather than energy transfer (ENT) pathway from [Ru(bpy)<sub>3</sub>]<sup>2+</sup> photosensitizer to ZIF-67 is the key parameter that controls the HER efficiency. Using in situ XAS, we identified the key intermediate species representing the rate limiting step in HER, a problem that has long plagued the catalytic community. These results represent a new level understanding of the interplay between the microscopic and macroscopic properties of ZIF-67, paving the way for their novel application in photocatalysis.

# 2. Materials and Methods

**ZIF-67 Synthesis.** ZIF-67 was synthesized according to our previous report<sup>29</sup> via a solution based method. Cobalt nitrate (Co(NO<sub>3</sub>)<sub>2</sub>·6H<sub>2</sub>O, Acros Organics) and 2-methylimidazole (C<sub>4</sub>H<sub>6</sub>N<sub>2</sub>, 97%, Alfa Aesar) were mixed in a 1:10 molar ratio in methanol at room temperature to give a violet precipitate that was washed thoroughly. Films were grown by the same method by immersing a quartz (Ted Pella Inc.) slide prior to mixing the Co and 2-methylimidazole precursors. The direct growth of ZIF-67 onto the slide was performed in three 1 hour steps where the slide was removed, rinsed with ethanol, and then re-immersed in fresh growth solution. After three growth steps, the backside of the film was wiped to mechanically remove the ZIF material to give a single ZIF-67 film on the front side.

[Ru(bpy)<sub>3</sub>]<sup>2+</sup> Synthesis. [Ru(bpy)<sub>3</sub>]<sup>2+</sup> was synthesized following the published literature procedure.<sup>30</sup> Commercial RuCl<sub>3</sub>·xH<sub>2</sub>O was dried in an oven at 120° C for 3 hours. Dried RuCl<sub>3</sub> (0.4 g, 1.93 mmol), 2,2'-bipyridine (0.9 g, 5.76 mmol), and water were placed in a 100 mL flask fitted with a reflux condenser. Sodium phosphinate was prepared by adding NaOH to 31% phosphinic acid until slightly cloudy precipitate is obtained, then re-adding phosphinic acid dropwise until the precipitate redissolves. Then, 2 mL of sodium phosphinate was added and the mixture was refluxed for 30 minutes. During reflux, the initial green solution changes color to brown and finally orange. The solution was filtered to remove traces of undissolved material, and then the crude product was precipitated by the addition of potassium chloride (12.6 g) to the filtrate. The solution and solid were then refluxed to give a deep red solution which, upon cooling to room temperature, yields brilliant red-orange crystals. The crystals were filtered, washed with ice-cold 10% aqueous acetone (2x5mL) and acetone (30 mL), and then air-dried.

**Photocatalytic HER Experiments.** HER photocatalysis was performed in glass vials of 9 mL volume with rubber septa. The stirred, N<sub>2</sub> purged vials were irradiated with 450 nm LEDs at

various power outputs, where the optimized power was 1.02 mW. The 400  $\mu$ L Headspace samples were analyzed for  $H_2$  concentration by an Agilent 490 micro gas chromatograph with 5 Å molecular sieve column.

**Standard Characterization.** UV-Visible measurements and diffuse reflectance measurements were performed on a Cary 5000 UV-VIS-NIR spectrophotometer with internal diffuse reflectance accessory. The XRD patterns were performed using a Rigaku Miniflex II XRD diffractometer with Cu Kα radiation. Emission spectrum of Ru(bpy)<sub>3</sub><sup>II</sup> in acetonitrile (ACN) was collected using a PTI QM40 spectrometer. Surface morphology of the thin film was characterized by a Bruker Dimension ICON AFM (Bruker, Santa Barbara).

Femtosecond Optical Transient Absorption (fs-OTA) Spectroscopy. A regenerative amplified Ti-Sapphire laser (Solstice, 1KHz repetition rate, 800 nm, <100 fs FWHM, 3.5mJ/pulse) provides the pump and probe pulses for fs-OTA measurements. The tunable (235-1100 nm) pump is generated by TOPAS from 75% of the Solstice output and is chopped at 500 Hz. The remaining 25% of Solstice output is used to generate white light in a sapphire crystal (420-800 nm) in a Helios ultrafast spectrometer (Ultrafast Systems LLC). The film sample on quartz substrate is translated continuously to avoid sample heating effects and sample degradation from the 410 nm pump pulses (0.75 μJ/pulse). The sample preparation for OTA was performed by immersing either a ZIF-67 (see ZIF-67 synthesis section) or Al<sub>2</sub>O<sub>3</sub> film (prepared as in our previous work)<sup>25</sup> in a 0.1M ethanolic solution of [Ru(bpy)<sub>3</sub>]<sup>2+</sup> for 30 minutes. The as-prepared film was then dried in air and used for OTA measurement. The 410 nm pump wavelength was chosen to selectively excite [Ru(bpy)<sub>3</sub>]<sup>2+</sup>, as neither bare ZIF-67 nor Al<sub>2</sub>O<sub>3</sub> gives transient signal under 410 nm excitation.

Nanosecond Optical Transient Absorption (ns-OTA) Spectroscopy. The ns-OTA measurements were performed at the Center of Nanoscale Materials at Argonne National

Laboratory. The tunable pump pulses from TOPAS are generated by a Ti-Sapphire laser system (Newport Spectra-Physics Spitfire Pro, 1.67 kHz repetition rate, 120 fs pulse). The fiber laser continuum probe was used to measure delay times out to 1 µs in an Ultrafast Systems EOS spectrometer. The same sample preparation as in fs-OTA was followed.

In Situ X-ray Absorption Spectroscopy (XAS). In Situ XAS was performed at beamline 12-BM at APS. The 3 mL catalysis mixture was sealed and N<sub>2</sub> purged in a custom Teflon cell with Kapton front window for X-ray irradiation and fluorescence emission and quartz rear window for photoirradiation. The X-ray fluorescence was detected by a Canberra 13-element geranium solid-state detector and the cell was irradiated from the rear window by the 450 nm LED at 1.02 mW power. The conditions for the *in situ* experiment were 1.25 M of TEOA, 4.5x10<sup>-4</sup> M of [Ru(bpy)<sub>3</sub>]<sup>2+</sup>, and 0.17 g/L ZIF-67 at a 3 mL reaction volume in acetonitrile with 5 mL headspace.

# 3. Results and Discussion

# 3.1. Synthesis and Characterization of ZIF-67.

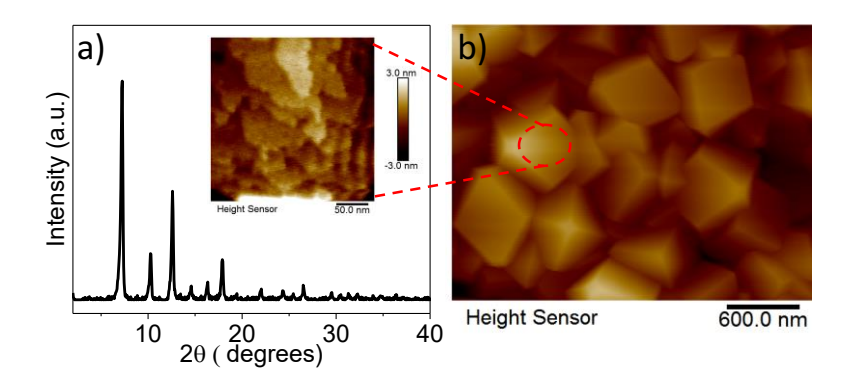


Figure 1. (a) Powder XRD patterns of ZIF-67. The inset shows the layered surface structure of ZIF-67 film. (b) AFM topography images of ZIF-67 thin film.

ZIF-67 was synthesized according to the established method from a methanolic mixture of cobalt(II) nitrate hexahydrate and 2-methylimidazole at room temperature.<sup>29</sup> The violet-colored powder product was confirmed to be ZIF-67 via XRD (Figure 1a), which shows good agreement to the published SOD-topology ZIF-67 pattern.<sup>6</sup> Using this protocol, the size of ZIF-67 crystallites is ~ 300-500 nm (Figure 1b) with layered structure on the surface (Inset of Figure 1a). The assynthesized samples can easily be suspended in solvent for catalytic application and mechanistic measurement.

# 3.2. ZIF-67 for Photocatalytic HER

Table 1. Optimization of conditions for ZIF-67 catalyzed HER with 6 mL volume (acetonitrile + TEOA) and 3 mL headspace, using 450 nm LED illumination for 48 hours.

Optimized Reagent (Fixed	Amount	μmoles H <sub>2</sub>	Activity
ZIF-67	0	0.12	-
$(1.25 \text{ M TEOA}, 2.2 \text{ x} 10^{-4} \text{ M})$	$1.7x10^{-2} \text{ g/L}$	0.854	8,540
	$8.3x10^{-2} \text{ g/L}$	2.85	5,730
$[Ru(bpy)_3]^{2+})$	$1.7x10^{-1} \text{ g/L}$	5.22	5,220
TEOA	0	0.005	50
$(1.7 \times 10^{-2} \text{ g/L})$	0.625 M	0.443	4,430
ZIF-67, 2.2 x10 <sup>-4</sup> M [Ru(bpy) <sub>3</sub> ] <sup>2+</sup> )	1.25 M	0.854	8,540
	2.5 M	0.362	3,620
$[Ru(bpy)_3]^{2+}$	0	0	0
(1.7x10 <sup>-2</sup> g/L ZIF-67, 1.25 M	$1.1x10^{-4} M$	0.384	3,840
TEOA)	$2.2 \times 10^{-4} M$	0.854	8,540
	$4.5 \times 10^{-4} \mathrm{M}$	$4.05^{a}$	$40,500^{a}$

<sup>&</sup>lt;sup>a</sup>3 mL reaction volume was used to increase the head space such that H<sub>2</sub> concentration does not exceed GC calibration.

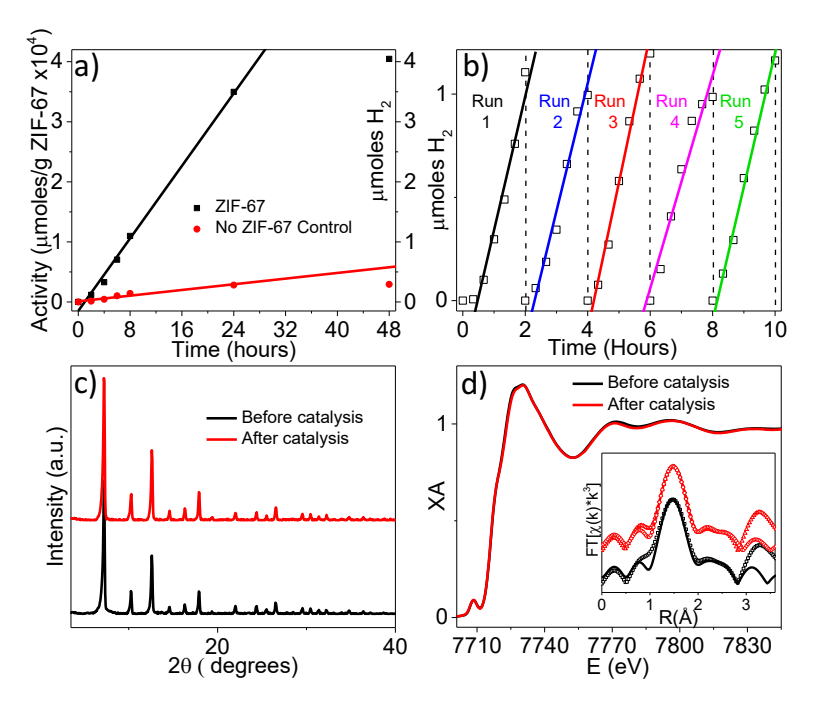


Figure 2. (a) The full-time profile of H<sub>2</sub> evolution under the optimized HER condition. (b) Recycling of ZIF-67 HER catalyst after multiple 2-hour experiments. (c) The comparison of XRD patterns of ZIF-67 before and after 5 catalytic cycles where after catalysis pattern was collected by using the same amount of ZIF-67 employed in before catalysis sample. (d) The comparison of ex situ XANES of ZIF-67 before and after catalysis. The inset compares the Fourier-transformed R-space data (open points) with their FEFF best fits (solid lines).

Photocatalytic performance of ZIF-67 for HER was examined upon illumination of a 450 nm LED light source in the presence of  $[Ru(bpy)_3]^{2+}$  as photosensitizer and triethanolamine (TEOA) as electron donor and proton source in acetonitrile solution. The reaction conditions were systematically optimized to identify the parameters for optimum HER activity in terms of catalyst. As shown in Table 1, while  $[Ru(bpy)_3]^{2+}$  alone can produce a small amount of  $H_2$  (0.12 µmoles), the amount of  $H_2$  generated significantly increases upon the addition of ZIF-67. Meanwhile, the control experiments in the dark or in the absence of  $[Ru(bpy)_3]^{2+}$  or TEOA yields negligible

amount of H<sub>2</sub>, suggesting the necessity of these components in HER. A series of experiments were also carried out by varying the concentrations of ZIF-67, [Ru(bpy)<sub>3</sub>]<sup>2+</sup>, and TEOA (Table 1), as well as LED powers (Table S1), from which an optimized condition, i.e. 1.7x10<sup>-2</sup> g/L of ZIF-67, 1.25 M of TEOA, 4.5x10<sup>-4</sup> M of [Ru(bpy)<sub>3</sub>]<sup>2+</sup>, and 1.02 mW of 450 nm LED power, was achieved.

The full time H<sub>2</sub> generation profile measured under the optimum catalytic condition is shown in Figure 2a. The system produces hydrogen steadily for the first 24 hours until the catalysis ceases at 48 hours, reaching an activity of 40,500 µmoles/g ZIF-67. The ZIF-67 catalyzed HER reaction was further investigated via recycling experiments, in which the ZIF-67 catalyst was centrifuged from the catalysis mixture, washed with ACN, and redispersed in a fresh catalysis mixture after every 2 hours of photocatalysis. As shown in Figure 2b, the catalytic activity remains similar within 5 cycles of experiment, suggesting that the catalyst is recyclable and remains active for at least 10 hours, consistent with the full-time profile experiment above.

The cease of catalysis can be attributed to the degradation of  $[Ru(bpy)_3]^{2+}$  as ZIF-67 retains its integrity while degradation of  $[Ru(bpy)_3]^{2+}$  was observed after catalysis. First, we observed that the original orange colored  $[Ru(bpy)_3]^{2+}$  in the system turns red-brown after being exposed to 450 nm LED light and the time-frame of this color change agrees well with the cease of catalysis. The red-brown colored products are likely permanently reduced  $[Ru(bpy)_3]^{2+}$ . As shown in Figure S1a, the UV-visible spectrum of  $[Ru(bpy)_3]^{2+}$  changes significantly after catalysis. The same change was observed in the sample where only  $[Ru(bpy)_3]^{2+}$  and TEOA are present in the solution (Figure S1b). As these changes agree well with that via electrochemical reduction of  $[Ru(bpy)_3]^{2+}$  (Figure S1c), it is likely that the color change of  $[Ru(bpy)_3]^{2+}$  after catalysis is due to permanent reduction of  $[Ru(bpy)_3]^{2+}$  by TEOA. While we are not sure of the exact degradation mechanism of  $[Ru(bpy)_3]^{2+}$ , it is possible that -bpy ligand substitution of reduced  $[Ru(bpy)_3]^{2+}$  by TEOA or its

degradation products may occur. This is because the reduction of Ru center typically leads to the destabilization of Ru-N bonds, which is then followed by ligand substitution by coordinating anionic or lewis basic species.<sup>31</sup> On the other hand, the integrity of ZIF-67 during catalysis was confirmed by comparing its structure before and after catalysis. As shown in Figure 2c, the XRD patterns of ZIF-67 before and after catalysis recycled from the reaction mixture remain unchanged, suggesting that HER does not disrupt the crystalline nature of ZIF-67. Furthermore, ex situ XAS was used to examine the effect of photocatalysis on the atomic-scale local structure about the Co nodes. As shown in Figure 2d, negligible difference was observed in the X-ray absorption near edge structure (XANES) spectra of ZIF-67 at Co K-edge before and after catalysis, suggesting that photocatalysis did not change the coordination geometry and oxidation state of Co nodes. This assignment was further supported by quantitative analysis of extended X-ray absorption fine structure (EXAFS) spectra (Figure S2) using FEFF fitting, where Co-N bond distance in beforeand after-catalysis samples remains same (within uncertainty) (inset of Figure 2d and Table S2).<sup>29</sup> These results suggest that both the local and bulk structure of ZIF-67 do not change after catalysis, indicating excellent stability of ZIF-67 during photocatalysis.

An additional concern to address is the possibility of leaching of Co into solution. By ICP-MS measurements, it was determined that 0.03 µmoles of Co are leached into solution during a 2-hour catalysis run in the recycling experiment. According to the Co(MIM)<sub>2</sub> equation, this represents approximately 0.3% leaching. In order to know the contribution of leached Co species to HER activity, we performed H<sub>2</sub> generation experiment of the supernatant solution under the same experimental conditions. The supernatant experiment gives negligible increase in HER activity compared to no ZIF-67 control condition, which suggests that leached Co species is not the active catalytic species, further supporting that ZIF-67 is the heterogeneous HER photocatalyst.

The HER activity observed for our ZIF-67 system is remarkable in comparison to other MOF systems for HER.  $^{32-43}$  In the absence of cocatalysts, the majority of these systems showed limited HER activity (0-10<sup>3</sup> µmol H<sub>2</sub>/g MOF). In the presence of cocatalysts, many of these systems demonstrated significantly boosted HER activity ( $10^2$ - $10^5$  µmol H<sub>2</sub>/g MOF). To best of our knowledge, the HER activity in our system (40,500 µmol/g ZIF) is indeed higher than the highest reported Pt containing MOF catalysts (~ 30,000 µmol/g MOF). The current ZIF-67 system, however, benefits from ease of synthesis and the prospect of scalability, as having intrinsically catalytic metal nodes means that there is no need for special cocatalyst treatments or addition steps. With respect to the catalytic Co metal nodes, using the Co(IM)<sub>2</sub> equation, a TON of 8 is calculated. While higher TONs ( $10^1$ - $10^3$ ) were reported in some cocatalyst-containing systems,  $^{34,44-46}$  these numbers were typically calculated with respect to cocatalyst instead of MOF. Indeed, the TON of our system is much higher than systems where TONs with respect to MOF (TON < 1) were reported.  $^{33,35,36}$ 

It is also noted that HER activity of ZIF-67 in the current system is  $\sim$  3 orders of magnitude higher than a similar system recently reported by our group, i.e. ZIF-67/RuN3 hybrid (48.5 µmol H<sub>2</sub>/g ZIF-67).<sup>25</sup> In that ZIF-67/RuN3 system, we have shown that enhanced HER activity can be attributed to efficient ENT from the excited RuN3 to ZIF-67, forming excited state ZIF-67. This leads to structural distortion of ZIF-67 accompanied with charge transfer from the imidazole ligand to Co center, ultimately resulting in H<sub>2</sub> production. The significantly enhanced HER activity in the current system using [Ru(bpy)<sub>3</sub>]<sup>2+</sup> as photosensitizer in comparison to the previous system with RuN3 as photosensitizer implies that the photocatalytic mechanism in the two systems is fundamentally different. In the following sections, we aim to fundamentally characterize the

distinct catalytic events and intermediate steps that contribute to ZIF-67 catalyzed HER by various spectroscopic means.

# 3.3. Light Harvesting and Charge Separation Dynamics in [Ru(bpy)<sub>3</sub>]<sup>2+</sup>/ZIF-67

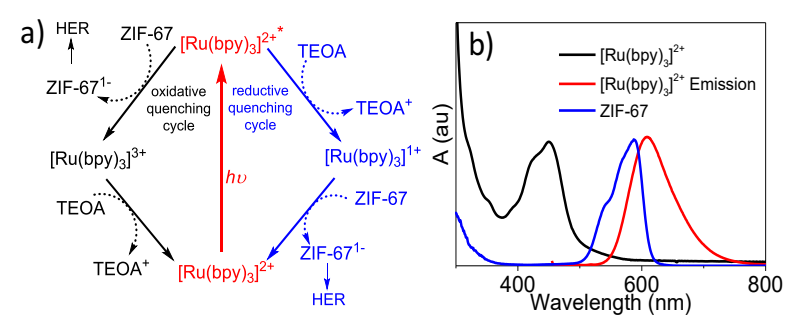


Figure 3. (a) Proposed catalytic mechanism of  $[Ru(bpy)_3]^{2+}/ZIF$ -67 for  $H_2$  generation. (b) The UV-Visible absorption spectra of  $[Ru(bpy)_3]^{2+}$  and ZIF-67, and the emission spectrum of  $[Ru(bpy)_3]^{2+}$ . The UV-visible absorption spectrum of ZIF-67 was collected in diffuse reflectance mode.

To fully understand the catalytic activity for HER observed, fundamental spectroscopic studies to elucidate the mechanism of interaction between the photosensitizer and ZIF-67 were performed. Due to the multicomponent nature of the photocatalytic system, there are multiple paths that could be followed to produce an activated ZIF-67 catalyst. The cartoon scheme in Figure 3a depicts these possibilities, namely A) the oxidative quenching cycle: ET from excited [Ru(bpy)<sub>3</sub>]<sup>2+</sup> to ZIF-67, forming the reduced ZIF-67 (ZIF-67<sup>1-</sup>) and oxidized [Ru(bpy)<sub>3</sub>]<sup>2+</sup> ([Ru(bpy)<sub>3</sub>]<sup>3+</sup>); the latter accepts an electron from TEOA and returns to its ground state while the former proceeds to catalytic reaction. B) the reductive pathway: ET occurs from TEOA to excited [Ru(bpy)<sub>3</sub>]<sup>2+</sup>, forming reduced [Ru(bpy)<sub>3</sub>]<sup>2+</sup> ([Ru(bpy)<sub>3</sub>]<sup>1+</sup>) and oxidized TEOA, which is followed by ET from ([Ru(bpy)<sub>3</sub>]<sup>1+</sup> to ZIF-67, forming ZIF-67<sup>1-</sup>. Another distinct possibility of ENT exists following our previous report of an ENT-based RuN3/ZIF-67 catalytic system.<sup>25</sup> Due to significant spectral

overlap between the emission spectrum of  $[Ru(bpy)_3]^{2+}$  and the absorption spectrum of ZIF-67 (Figure 3b) corresponding to the spin-allowed  ${}^4A_2(F)^{-4}T_1(P)$  d-d transition of Co, ENT process

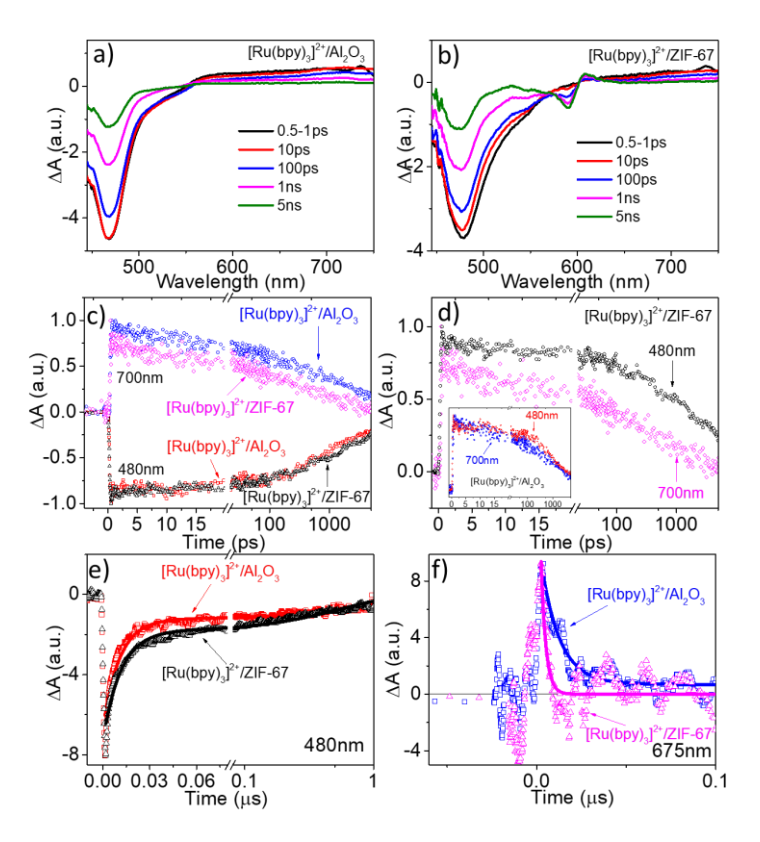


Figure 4. Femtosecond OTA results for selective excitation of [Ru(bpy)<sub>3</sub>]<sup>2+</sup> on Al<sub>2</sub>O<sub>3</sub> control (a) and ZIF-67 (b) at 410 nm. (c) The comparison of fs-OTA kinetics of [Ru(bpy)<sub>3</sub>]<sup>2+</sup> ES and GSB between Al<sub>2</sub>O<sub>3</sub> and ZIF-67. (d) The comparison of kinetics between ES and inverted GSB of [Ru(bpy)<sub>3</sub>]<sup>2+</sup> on ZIF-67 and on Al<sub>2</sub>O<sub>3</sub> (inset). Nanosecond OTA kinetics of the GSB recovery (e) and ES decay (f) on both substrates. Data is shown in open points and fits in solid lines.

from [Ru(bpy)<sub>3</sub>]<sup>2+</sup> to ZIF-67 is also feasible and needs to be considered. These photophysical and photochemical processes typically occur in ultrafast scale and have distinct spectral features, and can thus be distinguished using time-resolved optical spectroscopy.

Femtosecond optical absorption (fs-OTA) spectroscopy was first used to examine the ET/ENT dynamics between [Ru(bpy)<sub>3</sub>]<sup>2+</sup> and ZIF-67. Figure 4a and 4b show the fs-OTA spectra of

[Ru(bpy)<sub>3</sub>]<sup>2+</sup> on Al<sub>2</sub>O<sub>3</sub> and ZIF-67, respectively, after 410 nm excitation. 410 nm pump pulse was used to selectively excite [Ru(bpy)<sub>3</sub>]<sup>2+</sup> only, as [Ru(bpy)<sub>3</sub>]<sup>2+</sup> has prominent absorption at this wavelength while ZIF-67 has negligible absorption (Figure 3b). [Ru(bpy)<sub>3</sub>]<sup>2+</sup> on Al<sub>2</sub>O<sub>3</sub> substrate was used as control sample as neither ET nor ENT should occur from [Ru(bpy)<sub>3</sub>]<sup>2+</sup> to Al<sub>2</sub>O<sub>3</sub> due to extremely negative conduction band edge and large bandgap of Al<sub>2</sub>O<sub>3</sub>.<sup>47</sup> As shown in Figure 4a, the fs-OTA spectra of [Ru(bpy)<sub>3</sub>]<sup>2+</sup> on Al<sub>2</sub>O<sub>3</sub> show two instantaneously formed spectral features, including a negative feature centered at 480 nm and a broad positive feature from 565 nm to 750 nm. These features have been observed previously and can be attributed to ground-state bleach (GSB) of [Ru(bpy)<sub>3</sub>]<sup>2+</sup> and <sup>3</sup>MLCT excited state (ES) absorption formed through ultrafast intersystem crossing (ISC) after photoexcitation, respectively.<sup>47,48</sup> The recovery of GSB and decay of ES occur simultaneously with a clear isosbestic point at ~560 nm, suggesting that these dynamics represent the same recombination process, i.e. relaxation of ES molecules to their GS.

While the similar GSB and ES absorption of [Ru(bpy)<sub>3</sub>]<sup>2+</sup> on Al<sub>2</sub>O<sub>3</sub> are observed in the spectra of [Ru(bpy)<sub>3</sub>]<sup>2+</sup> on ZIF-67 (Figure 4b), two additional spectral features developed in the spectra of the latter, i.e. a negative feature at 580 nm and a positive absorption at 608 nm. These two features, resembling those observed previously in OTA spectra of ZIF-67 following direct excitation of ZIF-67,<sup>29</sup> can be attributed to the GSB and the formation of charge separated (CS) state in ZIF-67, respectively. Because no such features were observed in the fs-OTA spectra of ZIF-67 following 410 nm excitation, consistent with negligible absorption of ZIF-67 at 410 nm, the observed ZIF-67 features in the spectra of [Ru(bpy)<sub>3</sub>]<sup>2+</sup>/ZIF-67 must result from either ET or ENT from the excited [Ru(bpy)<sub>3</sub>]<sup>2+</sup>, which can be unambiguously distinguished by comparing the kinetic traces of [Ru(bpy)<sub>3</sub>]<sup>2+</sup> GSB and ES on each sample. If ENT is responsible for the formation of ZIF-67 features, one would expect a simultaneously enhanced recovery of GSB and decay of ES of

[Ru(bpy)<sub>3</sub>]<sup>2+</sup>, similar to our previous RuN3/ZIF-67 system.<sup>25</sup> However, as shown in Figure 4d, the decay of [Ru(bpy)<sub>3</sub>]<sup>2+</sup> ES occurs much faster than [Ru(bpy)<sub>3</sub>]<sup>2+</sup> GSB in [Ru(bpy)<sub>3</sub>]<sup>2+</sup>/ZIF-67 in contrast to the similar GSB and ES kinetics in [Ru(bpy)<sub>3</sub>]<sup>2+</sup>/Al<sub>2</sub>O<sub>3</sub> (Figure 4d, inset). Furthermore, while the GSB recovery of [Ru(bpy)<sub>3</sub>]<sup>2+</sup> in two samples remains similar, the ES decay in [Ru(bpy)<sub>3</sub>]<sup>2+</sup>/ZIF-67 sample is faster than that on Al<sub>2</sub>O<sub>3</sub>. These results, contradicting to the expected results for ENT, agree well with ET process from [Ru(bpy)<sub>3</sub>]<sup>2+</sup> to ZIF-67. As illustrated in Equation 1, ET results in the formation of [Ru(bpy)<sub>3</sub>]<sup>3+</sup> which facilitates ES decay and prohibits GSB recovery.

$$[Ru(bpy)_3]^{2+} * + ZIF - 67 \xrightarrow{ET} [Ru(bpy)_3]^{3+} + ZIF - 67^-$$
 (1)

The ET process was further confirmed by nanosecond OTA (ns-OTA) which allowed us to probe the ET dynamics at later time scale. The ns-OTA spectra for [Ru(bpy)<sub>3</sub>]<sup>2+</sup> on Al<sub>2</sub>O<sub>3</sub> and ZIF-67 (Figure S3) show similar spectral features to their fs-OTA spectra. However, from the kinetic traces (Figure 4e and 4f), it is apparent that while the ES of [Ru(bpy)<sub>3</sub>]<sup>2+</sup> decays faster on ZIF-67 than on Al<sub>2</sub>O<sub>3</sub>, the GSB recovery of [Ru(bpy)<sub>3</sub>]<sup>2+</sup> is slower in the former than the latter, further supporting our assignment of ET process from excited [Ru(bpy)<sub>3</sub>]<sup>2+</sup> to ZIF-67.

The observation of ET does not exclude the possibility of ENT to ZIF-67, as the emission of [Ru(bpy)<sub>3</sub>]<sup>2+</sup> has overlap with the absorption of ZIF-67 (Figure 3b). We are not able to examine ENT process by probing the emission of ZIF-67 because ZIF-67 is non-emissive in the visible range. However, according to the fact that the GSB recovery of [Ru(bpy)<sub>3</sub>]<sup>2+</sup> on ZIF-67 is slower while its ES decay is faster than that on Al<sub>2</sub>O<sub>3</sub>, we are able to estimate the upper limit rate for ENT process. The kinetics of [Ru(bpy)<sub>3</sub>]<sup>2+</sup> GSB recovery on ZIF-67 results from the combination of three possible paths, including 1) the intrinsic relaxation of ES molecules to GS, which follows the same GSB kinetics as on Al<sub>2</sub>O<sub>3</sub>; 2) the ENT process (if any), which is expected to enhance

GSB recovery with respect to GSB kinetics on Al<sub>2</sub>O<sub>3</sub>; and 3) the recombination of the oxidized [Ru(bpy)<sub>3</sub>]<sup>2+</sup> with the reduced ZIF-67 following ET process, which contributes to a slower GSB recovery on ZIF-67 than on Al<sub>2</sub>O<sub>3</sub>. Whether the GSB kinetics of [Ru(bpy)<sub>3</sub>]<sup>2+</sup> on ZIF-67 is faster or slower than that on Al<sub>2</sub>O<sub>3</sub> is determined by the competition between the 2<sup>nd</sup> and 3<sup>rd</sup> pathway. When the recombination through 3<sup>rd</sup> pathway is extremely slow and hardly contributes to the recovery of GSB, we can attribute the observed GSB recovery to ENT with an upper limit value of ENT rate. Through fitting the kinetic trace of [Ru(bpy)<sub>3</sub>]<sup>2+</sup> GSB recovery on ZIF-67 (Figure 4e), the obtained ENT time, which represents shortest ENT time constant, is 420 ns. Because this is much longer than the ES decay time (2.7 ns), obtained from fitting the ES decay kinetics of [Ru(bpy)<sub>3</sub>]<sup>2+</sup> on ZIF-67 (Figure 4f), we conclude that ENT process cannot compete with ET process. These results together suggest that photocatalysis proceeds through ET rather than ENT process from [Ru(bpy)<sub>3</sub>]<sup>2+</sup> to ZIF-67. This also explains why HER activity in the current system is orders of magnitude higher than RuN3/ZIF-67 system which mainly undergoes ENT process.

Given the beneficial ET process and high HER efficiency in the current [Ru(bpy)<sub>3</sub>]<sup>2+</sup>/ZIF-67 system, one would expect that [Ru(bpy)<sub>3</sub>]<sup>2+</sup> may link to ZIF-67 directly. However, we found that [Ru(bpy)<sub>3</sub>]<sup>2+</sup> can neither directly attach to the surface of [Ru(bpy)<sub>3</sub>]<sup>2+</sup>, nor can it enter the pore of ZIF-67 (Figure S4). While the origins of this problem remain uncertain to us, one possible explanation could be that [Ru(bpy)<sub>3</sub>]<sup>2+</sup> may be associated with ZIF-67 through electrostatic attraction, as the surface of ZIF-67 is terminated by imidazole ligands which exhibit anionic character. <sup>49</sup>

To reveal whether photocatalysis undergoes reductive or oxidative quenching cycle (Figure 3a), we measured the ET dynamics between TEOA and  $[Ru(bpy)_3]^{2+}$ , which can be evaluated by measuring the steady state emission intensity of  $[Ru(bpy)_3]^{2+}$  as a function of TEOA concentration.

As shown in Figure S5, the emission intensity of  $[Ru(bpy)_3]^{2+}$  is gradually quenched with increasing amount of TEOA added to the solution, suggesting that ET occurs from TEOA to  $[Ru(bpy)_3]^{2+}$ . The time constant for the emission quenching process was determined to be  $\sim 1.4 \, \mu s$  (details in SI), which is much longer than ET time from excited  $[Ru(bpy)_3]^{2+}$  to ZIF-67, suggesting that oxidative quenching cycle is the primary catalytic pathway for HER in the current  $[Ru(bpy)_3]^{2+}/ZIF$ -67 system.

## 3.4 In Situ XAS

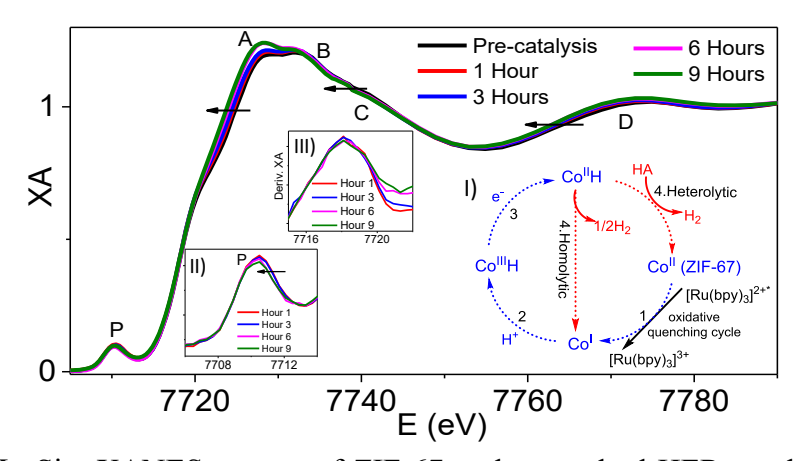


Figure 5. In Situ XANES spectra of ZIF-67 under standard HER condition. Inset I is the proposed catalytic mechanism for ZIF-67 catalyzed HER. Inset II is the zoom in picture of 1s-3d pre-edge feature. Inset III is the first derivative of XANES to illustrate the edge energy.

The time-resolved spectroscopic studies described above certainly provide important insight in the catalytic mechanism of the ZIF-67 catalysts, i.e. the light harvesting and charge separation (CS) dynamics which represents the key initial step to activate the catalytic cycle. However, many aspects of the mechanisms are yet unexplained. Besides the initial CS process (step 1 in inset I, Figure 5), the proposed catalytic pathway also involves the formation of hydride intermediates (step 2 and 3) which not only change the oxidation state (Co<sup>I-III</sup>) but also the coordination environment at Co center. The multiple intermediates formed at Co center are further complicated

by the possibilities of either homolytic or heterolytic H<sub>2</sub>-producing mechanisms (step 4).<sup>50</sup> As a result, it is necessary to experimentally characterize the intermediate states with a technique that can follow both the oxidation state and coordination/structure of the Co metal center during catalysis simultaneously, namely in situ XAS, to gain direct information of the function of the photocatalyst in real time.

In order to obtain significant XAS signal from Co, the proportion of ZIF-67 in the optimized catalysis mixture was increased to 0.5 mg in a 3 mL solution for in situ measurement, i. e. 10 times more ZIF-67 than that used in optimized condition. In contrast to immediate generation of H<sub>2</sub> under the optimized conditions, an induction period was observed under the in situ conditions (Figure S6). Because induction period was typically associated with the multiple equilibriums that require conversion of Co center to its reduced intermediates or hydrides before H<sub>2</sub> generation,<sup>25</sup> the presence of induction period in the in situ condition but not in the optimized condition is likely due to that longer time is required to convert larger amount of ZIF-67 to their intermediate species to achieve multiple equilibriums.

Figure 5 shows the in situ XANES spectra collected during the course of HER catalysis. The initial XANES spectrum shows a prominent pre-edge feature (labeled P) that corresponds to the dipole-forbidden 1s-3d transition due to p-d mixing in the non-centrosymmetric tetrahedral ligand field geometry. The two distinct rising edges at 7718 eV and 7724 eV are typical of Co<sup>II</sup> complexes with lower-order (<6) coordination.<sup>51</sup> In addition to these edge features, feature A and B, which correspond to the 1s-4p white line transition and are sensitive to coordination number at Co center, were also observed in the XANES spectra. During photocatalysis, multiple gradual changes to the XANES spectra are observed during the first 1-6 hours of illumination, which is consistent with the presence of induction period for H<sub>2</sub> generation. As seen from Figure 5, the overall spectrum

(A-D bands) shows a gradual red-shift, suggesting that Co-N bond distance increase during photocatalysis. This assignment was further supported by the pre-edge feature P which shifts to lower energy accompanied by the reduction of their intensity (Inset II). As pre-edge feature P is a measure of the ligand field strength at Co center,<sup>52</sup> the shift observed in P can be assigned to a decreased ligand field strength due to the elongation of Co-N bond. Furthermore, notable changes were observed in feature A and B, where the intensity of feature A increases while that of B decreases. As increased intensity for A and decreased intensity for B are responsible for a more highly-coordinated Co<sup>II</sup> center,<sup>51</sup> we believe that the coordination number of Co increases during catalysis. Despite these changes, negligible shift was observed in the edge region (Inset III), suggesting that the intermediate species remains +2 oxidation state.

While the above in situ XAS results unravelled that intermediate species possess larger coordination number and longer Co-N distance, and remain an oxidation state of +2, there are possibilities that such features could result from the average of multiple Co intermediates involved in the complex catalytic cycle (Inset I in Figure 5) or a single intermediate that accumulated during catalysis. If the former is responsible for the observed spectral features, the concentration of Co<sup>II</sup> and Co<sup>III</sup>H species (Inset I in Figure 5) is expected to remain similar during the catalytic cycle. In contrast, if the observed spectral features are mainly due to the accumulation of a single intermediate, this species is most likely Co<sup>II</sup>-H because this is the only Co<sup>II</sup> species in the proposed mechanism. As a result, the consumption of Co<sup>II</sup>-H (step 4) is possibly the rate limiting step in the photocatalytic cycle. It is also difficult to determine whether the homo- or heterolytic mechanism dominates in the catalytic cycle for ZIF-67 catalyzed HER. However, a requisite for the heterolytic mechanism is a highly acidic environment, <sup>50</sup> which is not present in the catalytic system, as TEOA is the proton source and has a 7.77 pKa in water. <sup>53</sup> Furthermore, the Co sites are confined to a

distance of approximately 6.00 Å in the crystal structure of ZIF-67.<sup>5</sup> Such short distance between Co sites make it possible that two Co<sup>II</sup>H species may interact within a single crystallite. These two factors together suggest that homolytic mechanism might be preferred in the current system, however, the heterolytic mechanism cannot be excluded.

#### 4. Conclusion

In summary, we report a recyclable and highly efficient ZIF-67 catalyst for HER. In the presence of molecular photosensitizer, we achieved an activity of 40,500 µmol H<sub>2</sub>/g ZIF, which is remarkable compared to other MOF H<sub>2</sub> evolution catalysts. More importantly, the mechanistic function for HER was investigated for the first time using time-resolved optical and real-time in situ XAS spectroscopic techniques. Using time-resolved OTA spectroscopy, we show that ET rather than ENT is the key factor that determines the efficiency of ZIF-67 for HER. Using in situ XAS, we uncovered the spectral features that correspond to the intermediate species for catalytic cycle, either resulting from the average of multiple intermediates or a Co<sup>II</sup>H species. These results not only demonstrate the potential of ZIF-67 as an intrinsic catalyst for HER, but also provide new insights for its further development.

As indicated by the charge separation pathway in this work, future work using photosensitizers that can facilitate ET but inhibit ENT process would certainly benefit HER efficiency. Inspired from the catalytic mechanism, future work should focus on the design of ZIF based catalytic systems with inherently large pore and cavity such that the key components for catalysis can be directly encapsulated, thereby making all catalytic metal sites accessible.

#### ASSOCIATED CONTENT

**Supporting Information.** Results for LED power optimization, the comparison of UV-visible spectra of catalysts before and after catalysis, spectroelectrochemistry data, the comparison of EXAFS of ZIF-67 before and after catalysis as well as FEFF fitting parameters, nanosecond OTA spectra, [Ru(bpy)<sub>3</sub>]<sup>2+</sup> emission quenching experiment, H<sub>2</sub> generation time profile for in situ XAS experiment are available free of charge via the Internet at <a href="http://pubs.acs.org">http://pubs.acs.org</a>."

#### **AUTHOR INFORMATION**

# **Corresponding Author**

\*Jier Huang (jier.huang@marquette.edu)

#### **Author Contributions**

The manuscript was written through contributions of all authors. All authors have given approval to the final version of the manuscript.

#### **Funding Sources**

This work was supported by National Science Foundation (DMR-1654140). Use of the Advanced Photon Source and nanosecond transient absorption spectroscopy at the Center for Nanoscale Materials in Argonne National Laboratory was supported by the U. S. Department of Energy, Office of Science, Office of Basic Energy Sciences, under Award No. DE-AC02-06CH11357.

### **ACKNOWLEDGMENT**

We thank Dr. Zhuangqun Huang's help in AFM measurements from the Molecular Materials Research Center of the Beckman Institute, California Institute of Technology.

#### REFERENCES

- (1) Phan, A.; Doonan, C. J.; Uribe-Romo, F. J.; Knobler, C. B.; O'Keeffe, M.; Yaghi, O. M. Acc. Chem. Res. **2010**, 43, 58-67.
- (2) Ray, K. G.; Olmsted, D. L.; Burton, J. M. R.; Houndonougbo, Y.; Laird, B. B.; Asta, M. Chem. Mater. **2014**, 26, 3976-3985.
- (3) Bux, H.; Feldhoff, A.; Cravillon, J.; Wiebcke, M.; Li, Y.-S.; Caro, J. Chem. Mater. **2011**, 23, 2262-2269.
- (4) Wu, T.; Feng, X.; Elsaidi, S. K.; Thallapally, P. K.; Carreon, M. A. Ind. Eng. Chem. Res. **2017**, 56, 1682-1686.
- (5) Banerjee, R.; Phan, A.; Wang, B.; Knobler, C.; Furukawa, H.; O'Keeffe, M.; Yaghi, O. M. Science **2008**, 319, 939-943.
  - (6) Chen, E.-X.; Yang, H.; Zhang, J. Inorg. Chem. **2014**, 53, 5411-5413.
  - (7) Ma, W.; Jiang, Q.; Yu, P.; Yang, L.; Mao, L. Anal. Chem. **2013**, 85, 7550-7557.
- (8) Lee, J.; Farha, O. K.; Roberts, J.; Scheidt, K. A.; Nguyen, S. T.; Hupp, J. T. Chem. Soc. Rev. **2009**, 38, 1450-1459.
- (9) Zhang, F.; Wei, Y. Y.; Wu, X. T.; Jiang, H. Y.; Wang, W.; Li, H. X. J. Am Chem. Soc. **2014**, 136, 13963-13966.
  - (10) Tran, U. P. N.; Le, K. K. A.; Phan, N. T. S. ACS Catal. **2011**, 1, 120-127.
- (11) Isimjan, T. T.; Kazemian, H.; Rohani, S.; Ray, A. K. J. Mater. Chem. **2010**, 20, 10241-10245.
- (12) Nguyen, L. T. L.; Le, K. K. A.; Truong, H. X.; Phan, N. T. S. Catal. Sci. Technol. **2012**, 2, 521-528.
- (13) Chizallet, C.; Lazare, S.; Bazer-Bachi, D.; Bonnier, F.; Lecocq, V.; Soyer, E.; Quoineaud, A. A.; Bats, N. J. Am Chem. Soc. **2010**, 132, 12365-12377.
  - (14) Nguyen, L. T. L.; Le, K. K. A.; Phan, N. T. S. Chinese J. Catal. **2012**, 33, 688-696.
- (15) Xamena, F. X. L. I.; Casanova, O.; Tailleur, R. G.; Garcia, H.; Corma, A. J. Catal. **2008**, 255, 220-227.
- (16) Zakzeski, J.; Debczak, A.; Bruijnincx, P. C. A.; Weckhuysen, B. M. Appl. Catal., A 2011, 394, 79-85.
- (17) Zhang, A. P.; Li, L. Q.; Li, J.; Zhang, Y.; Gao, S. Catal. Commun. **2011**, 12, 1183-1187.
- (18) Esken, D.; Turner, S.; Lebedev, O. I.; Van Tendeloo, G.; Fischer, R. A. Chem. Mater. **2010**, 22, 6393-6401.

- (19) Dang, T. T.; Zhu, Y. H.; Ngiam, J. S. Y.; Ghosh, S. C.; Chen, A. Q.; Seayad, A. M. ACS Catal. **2013**, 3, 1406-1410.
- (20) Jiang, H. L.; Liu, B.; Akita, T.; Haruta, M.; Sakurai, H.; Xu, Q. J. Am Chem. Soc. **2009**, 131, 11302-11303.
- (21) Kuo, C. H.; Tang, Y.; Chou, L. Y.; Sneed, B. T.; Brodsky, C. N.; Zhao, Z. P.; Tsung, C. K. J. Am Chem. Soc. **2012**, 134, 14345-14348.
  - (22) Dey, C.; Banerjee, R. Chem. Commun. **2013**, 49, 6617-6619.
  - (23) Wang, S.; Wang, X. Appl. Catal., B 2015, 162, 494-500.
- (24) Wang, S.; Yao, W.; Lin, J.; Ding, Z.; Wang, X. Angew. Chem. Int. Ed. **2014**, 53, 1034-1038.
- (25) Yang, S.; Pattengale, B.; Kovrigin, E. L.; Huang, J. ACS Energy Lett. **2017**, 2, 75-80.
  - (26) Wakerley, D. W.; Reisner, E. PCCP **2014**, 16, 5739-5746.
- (27) Popczun, E. J.; Read, C. G.; Roske, C. W.; Lewis, N. S.; Schaak, R. E. Angew. Chem. Int. Ed. **2014**, 53, 5427-5430.
- (28) Caban-Acevedo, M.; Stone, M. L.; Schmidt, J. R.; Thomas, J. G.; Ding, Q.; Chang, H.-C.; Tsai, M.-L.; He, J.-H.; Jin, S. Nat. Mater. **2015**, 14, 1245-1251.
- (29) Pattengale, B.; Yang, S.; Ludwig, J.; Huang, Z.; Zhang, X.; Huang, J. J. Am Chem. Soc. **2016**, 138, 8072-8075.
- (30) Lin, C. T.; Boettcher, W.; Chou, M.; Creutz, C.; Sutin, N. J. Am Chem. Soc. **1976**, 98, 6536-6544.
- (31) Xia, W.; Zhu, J.; Guo, W.; An, L.; Xia, D.; Zou, R. J. Mater. Chem. A **2014**, 30, 11606-11613.
- (32) Juris, A.; Balzani, V.; Barigelletti, F.; Campagna, S.; Belser, P.; Von Zelewsky, A. Coord. Chem. Rev. **1988**, 84, 85-277.
- (33) Horiuchi, Y.; Toyao, T.; Saito, M.; Mochizuki, K.; Iwata, M.; Higashimura, H.; Anpo, M.; Matsuoka, M. J. Phys. Chem. C **2012**, 116, 20848-20853.
- (34) Song, T.; Zhang, L.; Zhang, P.; Zeng, J.; Wang, T.; Ali, A.; Zeng, H. J. Mater. Chem. A **2017**, 5, 6013-6018.
  - (35) Kim, D.; Whang, D. R.; Park, S. Y. J. Am Chem. Soc. **2016**, 138, 8698-8701.
- (36) Wen, M.; Mori, K.; Kamegawa, T.; Yamashita, H. Chem. Commun. **2014**, 50, 11645-11648.

- (37) He, J.; Wang, J.; Chen, Y.; Zhang, J.; Duan, D.; Wang, Y.; Yan, Z. Chem. Commun. **2014**, 50, 7063-7066.
- (38) Yuan, Y.-P.; Yin, L.-S.; Cao, S.-W.; Xu, G.-S.; Li, C.-H.; Xue, C. Appl. Catal., B **2015**, 168–169, 572-576.
- (39) Pullen, S.; Fei, H.; Orthaber, A.; Cohen, S. M.; Ott, S. J. Am Chem. Soc. **2013**, 135, 16997-17003.
- (40) Fateeva, A.; Chater, P. A.; Ireland, C. P.; Tahir, A. A.; Khimyak, Y. Z.; Wiper, P. V.; Darwent, J. R.; Rosseinsky, M. J. Angew. Chem. Int. Ed. **2012**, 51, 7440-7444.
- (41) Zhou, T.; Du, Y.; Borgna, A.; Hong, J.; Wang, Y.; Han, J.; Zhang, W.; Xu, R. Eng. Environ. Sci. **2013**, 6, 3229-3234.
  - (42) Sasan, K.; Lin, Q.; Mao, C.; Feng, P. Chem. Commun. **2014**, 50, 10390-10393.
- (43) Zhang, Z.-M.; Zhang, T.; Wang, C.; Lin, Z.; Long, L.-S.; Lin, W. J. Am Chem. Soc. **2015**, 137, 3197-3200.
- (44) Nasalevich, M. A.; Becker, R.; Ramos-Fernandez, E. V.; Castellanos, S.; Veber, S. L.; Fedin, M. V.; Kapteijn, F.; Reek, J. N. H.; van der Vlugt, J. I.; Gascon, J. Eng. Environ. Sci. **2015**, 8, 364-375.
  - (45) Dongha, K.; Wang, D.R.; Park, S.Y. J. Am Chem. Soc. 2016, 138, 8698-8701.
- (46) Zhang, Z. M.; Zhang, T.; Wang, C.; Lin, Z. K.; Long, L. S.; Lin, W. B. J. Am Chem. Soc. **2015**, 137, 3197-3200.
  - (47) Wang, C.; deKrafft, K. E.; Lin, W. B. J. Am Chem. Soc. **2012**, 134, 7211-7214.
- (48) Shen, L. J.; Luo, M. B.; Huang, L. J.; Feng, P. Y.; Wu, L. Inorg. Chem. **2015**, 54, 1191-1193.
- (49) Kallioinen, J.; Benkö, G.; Sundström, V.; Korppi-Tommola, J. E. I.; Yartsev, A. P. J. Phys. Chem. B **2002**, 106, 4396-4404.
  - (50) Kalyanasundaram, K. Coord. Chem. Rev. 1982, 46, 159-244.
- (51) Tian, F.; Cerro, A.M.; Mosier, A.M.; Wayment-Steele, H.K.; Shine, R.S.; Park, A.; Webster, E.R.; Johnson, L.E.; Johal, M.S.; Benz, L. J. Phys. Chem. C, **2014**, 118, 14449-14456.
- (52) Dempsey, J. L.; Brunschwig, B. S.; Winkler, J. R.; Gray, H. B. Acc. Chem. Res. **2009**, 42, 1995-2004.
- (53) Della Longa, S.; Bianconi, A.; Palladino, L.; Simonelli, B.; Congiu Castellano, A.; Borghi, E.; Barteri, M.; Beltramini, M.; Rocco, G. P.; Salvato, B. Biophys. J. **1993**, 65, 2680-2691.
  - (54) Sarangi, R.; Cho, J.; Nam, W.; Solomon, E. I. Inorg. Chem. **2011**, 50, 614-620.
  - (55) Hall, H. K. J. Am Chem. Soc. **1957**, 79, 5441-5444.

# TOC IMAGE

